Astrophys Space Sci (2019) 364:127
https://doi.org/10.1007/s10509-019-3619-8

ORIGINAL ARTICLE

Dynamic patterns of self-organization inflow in collisionless magnetic reconnection

Chaoxu Liu[1] · Xueshang Feng[1] · Minping Wan[2] · Jianpeng Guo[3]

Received: 7 April 2019 / Accepted: 1 August 2019

Abstract We investigate the evolution of reconnection inflow using a fully kinetic approach. Three types of inflow are detailed, namely the collapse inflow, the vortex inflow and the reverse inflow. They are formed dynamically at different stages of reconnection via self-organizing processes, but are closely interrelated with each other. The reconnection starts from a small perturbation, which can trigger off a chain of pressure-induced collapses propagating into the inflow region. The pressure gradient results in the collapse inflow toward the reconnection site. Then due to the continuous injection of hot plasma carried by the reconnection outflows, the expanding exhaust causes its adjacent region to be compressed. The combined effects of the compression and the reflection of conducting walls lead to the formation of the vortex inflow. Subsequently, the reverse inflow develops gradually within the exhaust. Under the modulation of these inflows, the reconnection rate shows a transient oscillation. We also discussed the possible occurrence of the self-organization inflow available in different contexts.

Keywords Magnetic reconnection · Self-organization inflow · Kinetic simulation

✉ C. Liu
cxliu@swl.ac.cn

X. Feng
fengx@swl.ac.cn

1 State Key Laboratory of Space Weather, National Space Science Center, Chinese Academy of Sciences, Beijing 100190, China

2 Department of Mechanics and Aerospace Engineering, Southern University of Science and Technology, Shenzhen 518055, China

3 Planetary and Space Physics Group, Department of Astronomy, Beijing Normal University, Beijing 100875, China

1 Introduction

Magnetic reconnection can potentially cause many explosive phenomena such as magnetospheric substorms (Angelopoulos et al. 2008) and magnetic flux transfer events (Hasegawa et al. 2010; Øieroset et al. 2011; Liu et al. 2017a). Reconnection starts from a small diffusion region where some non-ideal physical effects play a role, the effects may originate from the enhanced resistivity (Ugai 1984), the collisionless effects (Mandt et al. 1994; Shay and Drake 1998; Birn et al. 2001, Ma et al. 2001), and the plasmoid instability related to the Hall effect (Huang et al. 2011). The resultant fast magnetic reconnection has a typical rate of $0.1V_A$ (Liu et al. 2017b). In general, the reconnection rate that measures the conversion efficiency of magnetic to plasma energy in the reconnection diffusion region will undergo periods of rising, quasi-steady or falling (Fujimoto 2006; Lu et al. 2013). In addition to the effects in the diffusion region, the studies suggest that the sufficiency of the inflow is crucial for the growth of the reconnection rate and maintains the steady-state reconnection (Matthaeus 1982; Jin et al. 2005; Wan et al. 2008; Lapenta 2008).

Reconnection inflow can be maintained with the external driving forces (Jin et al. 2005; Liu et al. 2013) or the dynamics of reconnection itself (Matthaeus 1982; Shay and Drake 1998; Birn et al. 2001; Daughton et al. 2006; Fujimoto 2006; Lapenta 2008; Karimabadi et al. 2011). In driven reconnection simulations, the driving force is applied to the top and bottom boundaries of the system. Plasma inflows generated through the $E \times B$ drift move towards the reconnection region. The applied electric field (E) may be inspired by the cross-tail electric field in the Earth's magnetotail (Liu et al. 2013). In the absence of external driving forces, the formation of inflows is caused by the self-organizing process of reconnection. The trigger of the inflow usually originates from

Published online: 08 August 2019

the effects of perturbation as used in the GEM reconnection challenge (Birn et al. 2001), the perturbation destroys the pressure equilibrium in the current sheet and promotes the development of the inflow. In addition, the simulations show that the reconnection outflow can evolve into the closed-circulation pattern in multiple X line reconnection. The circulation flows carry the magnetic flux towards the reconnection region and promote the fast reconnection as they plunge down (Matthaeus 1982; Lapenta 2008). Especially when the two reconnection sites are close to each other, the reconnection outflows may meet at the centre of the magnetic flux rope, thus affecting the topology of the magnetic field (Liu et al. 2017a). The reconnection outflows with opposite directions, originating from two adjacent sites, are often observed by multiple spacecraft within the magnetic flux ropes (Hasegawa et al. 2010; Øieroset et al. 2011).

In situ measurements of magnetic reconnection, however, the reconnection rate often shows an oscillation with varying amplitudes, implying that the actual reconnection could be a transient process that involves multiple inflow regimes. This paper presents the dynamic patterns of reconnection inflow based on two-dimensional fully kinetic simulations. In the simulations, we consider the effect of self-organization in the spontaneous reconnection on the transition of the inflow. Three different types of inflow have been detailed, namely the collapse inflow, the vortex inflow and the reverse inflow appearing in the long-term evolution of reconnection. They are self-organized at different stages of reconnection and have their own unique patterns of formation and evolution, but are closely interrelated with each other. The time-varying reconnection rate associated with these inflows are also examined.

The remainder of the paper is organized as follows. In Sect. 2, the simulation model is described. Section 3 presents the simulation results, and Sect. 4 contains the summary and discussion.

2 Simulation model

The simulation is performed with the electromagnetic particle-in-cell (PIC) code pCANS. In the PIC algorithm the time-dependent part of Maxwell's equations are solved on the mesh by using an implicit scheme (Hoshino 1987):

$$\frac{\partial \boldsymbol{B}}{\partial t} = -c\nabla \times \boldsymbol{E}, \tag{1}$$

$$\frac{\partial \boldsymbol{E}}{\partial t} = c\nabla \times \boldsymbol{B} - 4\pi \boldsymbol{J}, \tag{2}$$

where $\boldsymbol{E}$ and $\boldsymbol{B}$ are the electric and magnetic fields, c and $\boldsymbol{J}$ are the speed of light and the current density. The finite-difference time-domain (FDTD) method is employed to ensure that the current continuity equation remains valid on the spatial grid. The particle dynamics is governed by the Newton-Lorentz equations of motion:

$$\frac{d\boldsymbol{x}_p}{dt} = \boldsymbol{u}_p, \tag{3}$$

$$\frac{d\boldsymbol{u}_p}{dt} = \frac{q_s}{m_s}\left(\boldsymbol{E} + \frac{\boldsymbol{u}_p}{c} \times \boldsymbol{B}\right), \tag{4}$$

where $\boldsymbol{x}_p$ and $\boldsymbol{u}_p$ are the position and velocity of each particle p. The charge to mass ratio (q_s/m_s) has the same value for each species s. The charge and current densities $(\rho_s, \boldsymbol{J}_s)$ on the grid are obtained by:

$$\rho_s = \sum_{p=1}^{N_s} q_s S(\boldsymbol{x} - \boldsymbol{x}_p), \tag{5}$$

$$J_s = \sum_{p=1}^{N_s} q_s u_p S(\boldsymbol{x} - \boldsymbol{x}_p), \tag{6}$$

where $S(\boldsymbol{x} - \boldsymbol{x}_p)$ is the shape function of the particles, and the sums are calculated over all particles N_s.

The simulation starts with the Harris equilibrium (Harris 1962) in the xz plane and the magnetic field configuration is $B(z) = B_0 \tanh[(z - L_z/2)/\lambda]$, where $\lambda = 0.5d_i$ determines the half-thickness of the initial current sheet. The corresponding density distribution is $n(z) = n_0 \mathrm{sech}^2[(z - L_z/2)/\lambda] + n_b$, and $n_b = 0.2n_0$ represents a uniform background plasma without drift velocities. The current-sheet plasma, $n_0 = {B_0}^2/(8\pi RT_0)$ (R is the gas constant), is treated as a drifting Maxwellian distribution. Other plasma parameters are the ion-electron mass ratio $m_i/m_e = 100$, temperature $T_i/T_e = 5$, and $\omega_{pe}/\Omega_{ce} = 2$, where ω_{pe} and Ω_{ce} are the electron plasma frequency and gyro-frequency. The speed of light c is set as $20V_A$, where $V_A = B_0/\sqrt{4\pi m_i n_0}$ is the Alfvén speed.

The simulation domain ($L_x \times L_z = 32d_i \times 16d_i$) is divided into 1024×512 grid points, where $d_i = c/\omega_{pi}$ is the ion inertial length based on n_0. Thus the spatial resolution is $\Delta x = \Delta z = 0.03125d_i$, and the electron Debye length is $\lambda_{De} = 0.46\Delta x$. The time step is $\Delta t\Omega_{ci} = 0.001$, and Ω_{ci} is the ion plasma gyro-frequency. The resolution allows us to retain electron kinetic effects accurately at multiple spatial and temporal scales. Here we use more than 1.2×10^7 particles for each species (ion and electron). The density decomposition scheme (Esirkepov 2001) is applied to exactly maintain the charge conservation for simulation particles.

In all runs, the periodic boundary conditions are employed in the x direction and the ideally conducting walls are imposed at the z boundaries. In order to promote the development of the initial equilibrium into the nonlinear regime, we consider a small flux perturbation (Treumann et al. 2010) imposed on the centre of the computational domain, with $\delta A_y = -0.12\lambda B_0 \exp[-(x^2 + z^2)/(2\lambda)^2]$.

3 Simulation results

At the starting of the equilibrium state, we put the localized perturbation in the current sheet to seed reconnection onset. The mechanism of reconnection onset remains a topic of debate in the plasma physics community. In the present study, the emphasis is paid on the nonlinear evolution of the reconnection process after the onset. In the following subsections, after showing the temporal evolution of the reconnection rate, we investigate the dynamic patterns of inflow formed at different states of the reconnection via self-organizing process.

3.1 Temporal evolution of the reconnection rate

The temporal evolution of the reconnection rate, $\partial A/\partial t$, is plotted in Fig. 1. Here the magnetic flux function $A(t, x, z)$ is measured at the X-line. The dot-dashed lines in Fig. 1 show the significant moments $(t_1, t_2, t_3, t_4, t_5)$ defined by the peak-valley or reversal points of the reconnection rate. In the present case without any external driving forces, the rate displays a typical non-steady reconnection variation. The onset of reconnection occurs at around $t\Omega_{ci} = 4$, after the imposed initial perturbation. Then the reconnection rate quickly reaches its maximum value of 0.24 at $t_1\Omega_{ci} = 11$. During the interval $4 \sim t_1\Omega_{ci}$, the reconnection rate continues to grow with different speed as indicated by the slope of the curve. From the turning point $t\Omega_{ci} = 7$, the reconnection rate begins to increase more quickly with time. After the first peak ($t_1\Omega_{ci}$), the rate decreases quickly until reaching a valley value at $t_2\Omega_{ci} = 22$. The time taken to reach the valley is $11\Omega_{ci}^{-1}$. Again, the rate goes through a new round of rising and falling cycle during the interval $t_2\Omega_{ci} \sim t_4\Omega_{ci}$. The second peak (at $t_3\Omega_{ci} = 24$) has a value of 0.16, which is much smaller than that of the first one. The temporal evolution of the rate behaves self-similarly to a certain extent between the two cycles ($0 \sim t_2\Omega_{ci}$ and $t_2\Omega_{ci} \sim t_4\Omega_{ci}$). Note

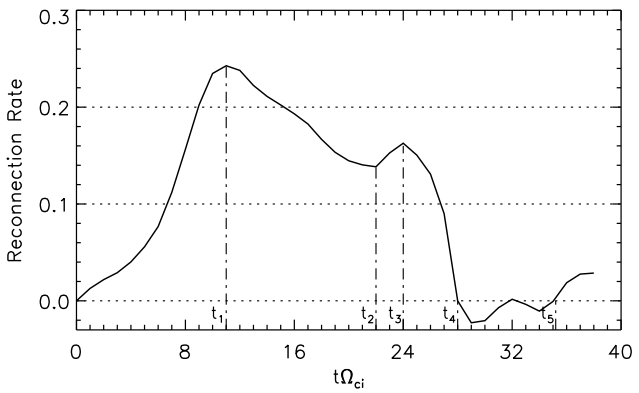

Fig. 1 The time history of the reconnection rate, $\partial A/\partial t$. The dot–dashed lines show the significant moments $(t_1, t_2, t_3, t_4, t_5)$ of the reconnection rate variation

that the reconnection rate switches from positive to negative at $t_4\Omega_{ci} = 28$. Following Cai et al. (1997) we refer to this process as "reverse magnetic reconnection" with typical characteristics of $E \cdot J < 0$ near the X-line, during which kinetic energy could be converted into magnetic energy. As shown in Fig. 1, the reverse reconnection occurs mainly during the period from $t_4\Omega_{ci}$ to $t_5\Omega_{ci}$. Meanwhile, the bouncing phenomenon of the reconnection rate can be seen, suggesting that the pressure imbalance exists along the outflow direction between the plasma and the magnetic field. After $t_5\Omega_{ci} = 35.2$, the reconnection reenters the normal model. Taken together, the reconnection rate presents a remarkable oscillation with time-varying amplitude. Furthermore, in terms of the reconnection rate variation, three types of inflow are presented and analyzed in detail, including the evolution and origin of these inflows and how they affect the reconnection rate. They are formed spontaneously at different periods of development based on the simulations.

3.2 Collapse inflow

The first type of inflow (called collapse inflow hereafter) occurs mainly during the interval $0 \sim t_2\Omega_{ci}$. Figure 2a shows a snapshot of the collapse inflow, where the contour of the velocity component V_{iz} is plotted at $t_1\Omega_{ci}$. The region of enhanced inflow has a fan-shaped distribution, as shown by distinct colors within the circle. The maximum inflow of 0.3 is found in two concentric arcs with the same radius of $1.6d_i$ away from the X-line. The edge region of inflow fan expands outward in the radial direction as the reconnection evolves. The expanding process is inhibited after $t\Omega_{ci} = 14$ due to the limited z boundaries, but it continues to expand along the x direction. The above fan region is formed only after $t\Omega_{ci} = 7$. During the interval from 0 to 7, the distribution of sign-alternating V_{iz} is observed along the z direction. With the driving of the collapse inflow, the magnetic reconnection occurs continuously. The magnetic configuration of reconnected field lines is shown in Fig. 2b. Figure 2c is the contour of the out-of-plane field B_y, where the dashed line denotes the magnetic separatrix. The origin of the collapse inflow comes from a chain reaction of pressure imbalance.

To further understand the origin of the collapse inflow, we plot the contour of the magnetic pressure in Fig. 3a. At the initial stage, the reconnection is triggered in the current sheet with the magnetic flux perturbation added to the centre of the computational domain. The topology of the magnetic field displays an X-shaped structure in the diffusion region (Fig. 2b). The plasma is then drained away from this region and ejected into the exhaust region under the magnetic tension of X-shaped field lines. This process results in a plasma depletion layer in the diffusion region (Øieroset et al. 2001; Yang et al. 2006), where the equilibrium between the thermal and magnetic pressures is destroyed. Then the

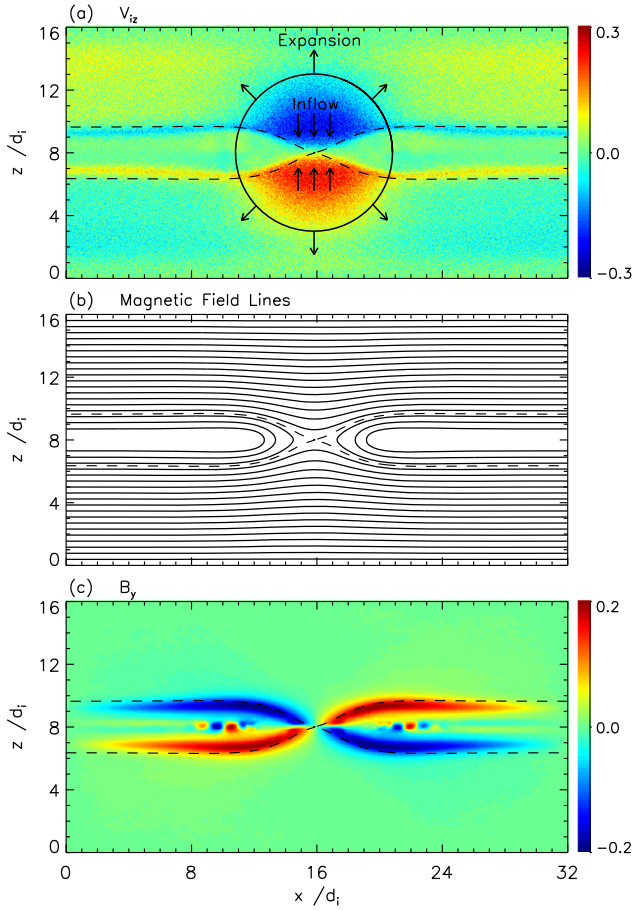

Fig. 2 (**a**) The contours of V_{iz}, (**b**) the magnetic field configuration (solid line), and (**c**) the out-of-plane field B_y at $t_1\Omega_{ci}$, the dashed line marks the magnetic separatrix

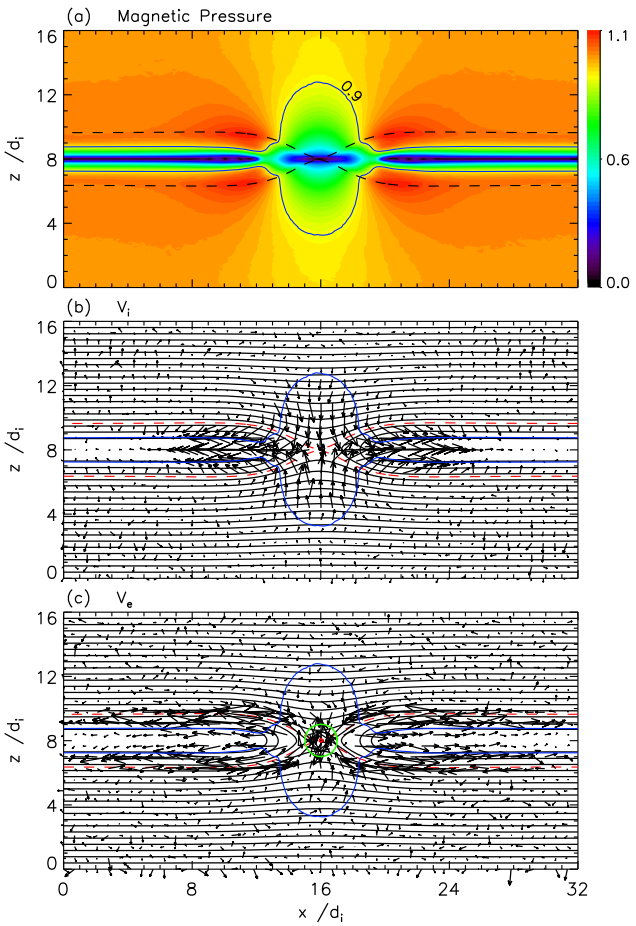

Fig. 3 (**a**) The contour of the magnetic pressure, the distribution of ion (**b**) and electron (**c**) velocity (arrows) with the magnetic field lines (solid line). The green-red circle encircles the area with the radius of ion-electron inertia length

surrounding plasma surges into the depletion layer from the upstream region under high-pressure conditions. This chain reaction is similar to toppling dominoes spreading outward from the diffusion region with a fan-shaped radiation path. Correspondingly, the plasma inflow formed in the upstream region is called the collapse inflow (Figs. 3b and 3c). The collapse inflow carries the upstream magnetic flux toward the reconnection region, thus the distribution of decreasing magnetic pressure can be observed in the upstream region (see Fig. 3a). To sum up, once the local perturbation is activated in the current sheet, the initial pressure balance will be broken there. The perturbation propagates outwards with time, giving rise to the collapse inflow from the inflow region. Such perturbation may originate from the instability of the current sheet, such as the Weibel instability described by Treumann et al. (2010)

Driven by the collapse inflow, the reconnection develops rapidly in the diffusion region. The initial growth of the reconnection is provided by the tearing mode instability, but the instability would tend to saturate at low levels. The reconnection enters a rapid growth phase after $t\Omega_{ci} = 7$ when the Hall effect starts to work in the reconnection layer (Mandt et al. 1994; Birn et al. 2001; Ma and Bhattacharjee 2001). Correspondingly, the reconnection rate increases rapidly (see the interval $8 \sim t_1\Omega_{ci}$ in Fig. 1). The role of the Hall effect is illustrated in Figs. 3b and 3c, where the ion-electron velocity vector is expressed with the black arrows. The solid lines are the magnetic field lines, and the area with the radius of ion-electron inertia length is encircled by the green-red circle (Fig. 3c). With the collapse inflow, the magnetic flux is transported into the reconnection region. The ions become demagnetized within the ion inertial region, while the electrons carrying the magnetic flux will continue to move inward. The separation of ion-electron motion results in the Hall current and the corresponding electromagnetic fields. Compared with the ions, the electrons have a higher flux-transport efficiency because of their relatively smaller inertial mass. Thus the reconnection rate has a rapid increase accordingly. Here the newly connected magnetic field lines are dragged out of the reconnection plane by the electrons (Mandt et al. 1994), result-

ing in the formation of the quadrupole Hall magnetic field (Fig. 2c). The resistance will therefore be reduced with the decrease of magnetic-field accumulation within the outflow region near the X-line (Karimabadi et al. 2011), promoting the development of fast reconnection. In addition, the finiteness of the inflow region can affect the supply of the collapse inflow, which is elaborated in the next subsection.

3.3 Vortex inflow

The second type of inflow (called vortex inflow) occurs mainly during the interval $t_1\Omega_{ci} \sim t_3\Omega_{ci}$. Figure 4a shows the plasma flow pattern with the magnetic field lines at time $t_3\Omega_{ci}$. Two vortex pairs are observed in the upstream region of reconnection, and they exhibit an approximate mirror-symmetry with respect to the x-axis. In the upper left quadrant, the vortex appears in clockwise order with its core close to the separatrix. The left part of the vortex rotates toward the wall boundary, while the right part moves toward the reconnection region. Thus in the inflow region the newly formed vortex inflow merges with the original collapse inflow. The maximum velocity of 0.26 is located on the vortex edge. The streamline map in Fig. 4b shows the overall configuration of the vortex pairs more clearly.

The vortex inflow can occur naturally when the reconnection process develops to a certain stage. The formation of vortices usually requires the plasma flow to be tightly coupled along mutually perpendicular directions. Here, the reconnection outflow jets within the exhaust region provide

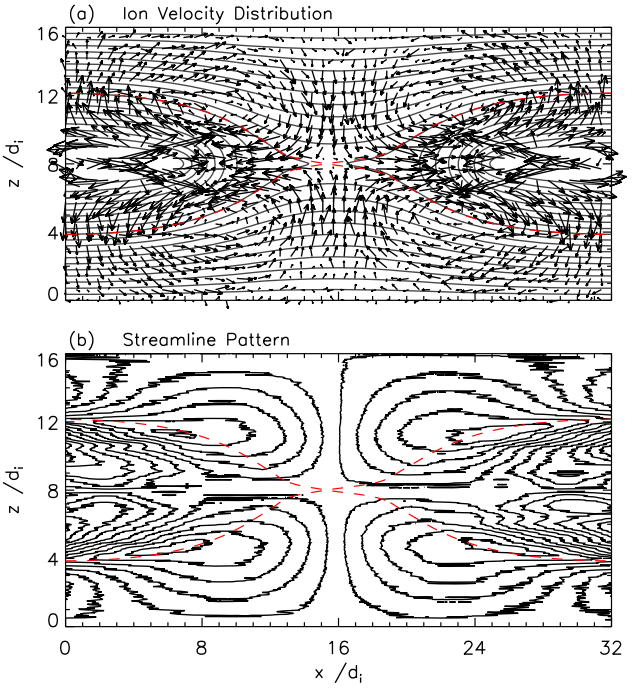

Fig. 4 (**a**) The distribution of ion velocity with the magnetic field lines, (**b**) the streamline map of the vortex pairs at $t_3\Omega_{ci}$

the main driving force for the parallel motion of the vortices. Meanwhile, the hot plasma is injected into the exhaust region by the reconnection outflow, leading to the rapid expansion of the exhaust region due to the enhanced plasma pressure. The expanding exhaust causes its adjacent inflow region to be compressed. The combined effects of expansion and compression lead to the formation of vertical plasma transport in the inflow region (see the upper left corner in Fig. 4a). Two vortex pairs develop gradually under the coupling actions of the parallel and perpendicular movements, as depicted in Fig. 4. Besides the above-mentioned movements, two other factors also contribute to the formation of the vortex flow. One is the effect of inhomogeneous expansion within the exhaust region, especially in the central part with the fastest expansion rate. The expansion causes the plasma in the vicinity of the separatrix to be compressed in the vertical direction and to be rolled up simultaneously. The second is the reflection effect of the conducting walls. The plasmas are reflected back into the inflow region when they reach the z boundaries.

The resulting confluence of the collapse inflow and the vortex inflow pushes the reconnection rate to renewed growth. Compared with small-scale vortices, large vortices need more time to develop in the simulation. Therefore, it will also take a long time to realize the influence of the vortex inflow on the reconnection rate. The variation of the reconnection rate during the interval $t_2\Omega_{ci} \sim t_3\Omega_{ci}$ (see Fig. 1) is mainly influenced by the vortex inflow. The vortex inflow reaches the reconnection region from $t_2\Omega_{ci}$, which drives the reconnection to occur and makes the reconnection rate increase again. At about $t_3\Omega_{ci}$, the reconnection rate reaches its second peak that is smaller than the first peak in magnitude. In theory, the vortex inflow is expected to boost the development of fast reconnection. Compared to the collapse inflow, the vortex inflow can more efficiently carry the magnetic flux toward the reconnection region from the broad inflow region. However, the vortex inflow exists in a relatively short period of time due to the appearance of the reverse inflow (see the next subsection in detail). Subsequently, the reconnection rate decreases sharply after the collapsing of the large-scale vortex structures.

3.4 Reverse inflow

At $t_4\Omega_{ci} = 28$, the reconnection rate switches from positive to negative, indicating that the reverse reconnection occurs. During the reverse reconnection, the plasma kinetic energy is converted into the magnetic energy locally. The transformation of reconnection pattern mainly results from the effect of the periodic boundary conditions by which the reconnection outflow changes its direction and enters into the diffusion region. The newly generated inflow is referred to as the reverse inflow for convenience. The distribution of

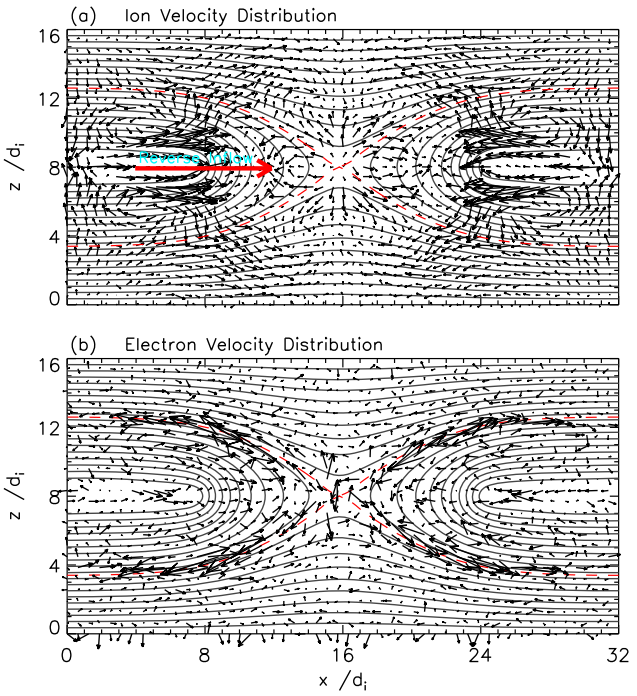

Fig. 5 (**a**) The distribution of ion velocity with the magnetic field lines, (**b**) electron velocity at $t\Omega_{ci} = 28$

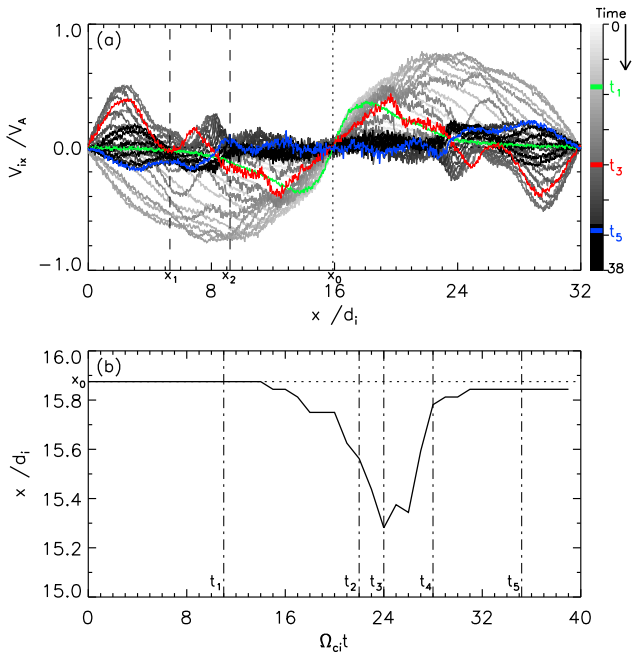

Fig. 6 (**a**) The time variation sequence of the velocity component V_{ix} along $z = 8d_i$, (**b**) the location of the X-line varies with time

this type of inflow at $t_4\Omega_{ci}$ is shown in Fig. 5. The ion and electron flows, V_i and V_e, are plotted with magnetic field lines (solid lines). In Fig. 5a, overlooking the ion velocity vector within the exhaust region enclosed by the magnetic separatrix (red dashed lines), we can find the reverse inflow (red arrow) moves toward the X-line. The maximum speed of the inflow ($V_i|_{max} = 0.63$) appears at the central region of the exhaust region. Driven by the reverse inflow, the reverse reconnection occurs continuously near the site of the original X-line. The newly outflow and the original vortex inflow continue to confront each other in the inflow region. The corresponding electron velocity has the same distribution, but the high-velocity electron flows are more concentrated around the separatrix.

The formation process of the reverse inflow is shown in Fig. 6a, where the time variation sequence of the velocity component (V_{ix}) is plotted. The velocity curves of $t_1\Omega_{ci}$, $t_3\Omega_{ci}$ and $t_5\Omega_{ci}$ are marked by distinct colors (green, red and blue). At $t_1\Omega_{ci}$, the reconnection outflows (green line) are ejected from the reconnection site ($x = x_0$) to the left and right boundaries ($x = 0, 32$), which is also known as the centre of the magnetic island in the context of multiple X-line reconnection. After a certain distance from the reconnection site, the reconnection outflows will collide head-on in the centre region, causing the outflows turn their directions as shown by the red curve of $t_3\Omega_{ci}$. Thus the reverse inflow is gradually emerging in the central region ($0 \sim x_2$) and moves toward the reconnection site during the interval $t_3\Omega_{ci} \sim t_5\Omega_{ci}$.

Driven by the reverse inflow, the reconnection rate changes with time. Two aspects of the changing trends are worth mentioning. First, the reconnection rate decreases rapidly from $t_3\Omega_{ci}$ and becomes negative at $t_4\Omega_{ci}$. During this period, the left drift of the X-line is suppressed (see Fig. 6b where shown the location of the X-line varies with time). At $t_4\Omega_{ci}$, the X-line drifts to the position of $x = 15.78d_i$ close to x_0. Second, the reverse reconnection with the negative reconnection rate occurs during the interval $t_4\Omega_{ci} \sim t_5\Omega_{ci}$. The reverse inflow carries the magnetic field lines towards the reconnection site. The magnetic field lines with high tension piles up near the reconnection region. In this way the kinetic energy of the reverse inflow is converted into the magnetic energy, similar to the process of pulling a slingshot. The increasing magnetic field tension will impede the movement of the reverse inflow towards the reconnection region. The dynamic imbalance between the magnetic field tension and the reverse inflow could lead to the bouncing phenomenon of the reconnection rate (see the interval $t_4\Omega_{ci} \sim t_5\Omega_{ci}$ in Fig. 1). As a result of the conflict the direction of plasma inflow constantly changes near the x_1 position. At $t_5\Omega_{ci}$ (the blue line in Fig. 6a), a equilibrium state is obtained. After that, the normal reconnection begins to occur.

4 Summary and discussion

In this paper, we use the fully kinetic approach to investigate the dynamic patterns of the reconnection inflow. Three

types of inflow, the collapse inflow, the vortex inflow and the reverse inflow, are analyzed in detail. They are formed by self-organization during different stages of reconnection, but are closely interrelated with each other. Driven by these inflows, the resultant reconnection rate is modulated over time and shows an oscillating behavior.

Although the simulations show that the inflows are related to each other through the cross-coupling of the flow, they can occur independently in different reconnection contexts. In the solar wind plasma, the reconnection may be trigged by a locally enhanced resistivity (Vasyliunas 1975). Therefore, the collapse inflow could be occurred under this context. In the magnetosphere, the driven reconnection is often observed, and the driving forces could originate from the solar wind for the magnetopause environment (Hasegawa et al. 2010) or the tail-crossing electric field for the magnetotail (Liu et al. 2013). After the onset of reconnection, as proposed by Matthaeus (1982), the localized vorticity near the X-point can affect the reconnection rate through a dynamical process. These quadrupole-like vorticity amplifies the inflow intensity, boosting the reconnection rate. In return, the current filament of the reconnection region promotes the further growth of vorticity with $B \cdot \nabla J$, where B is the background field. This nonlinear process develops in the way of positive feedback (see Fig. 6 in Matthaeus 1982) until the vorticity convects downstream. In open environments, such as the magnetosphere, the vorticity is easily convected away from the reconnection region. Thus the vortex flows need to be generated continuously to maintain fast reconnection (Lapenta 2008). In this study, the formation of the vortex inflow is similar to that of the theoretical analysis given by Matthaeus 1982. In addition to the elongation of vortices along the magnetic separatrices, several factors also influence the evolution of the vortex inflow, including the expansion of the exhaust region, the periodic boundary conditions, and the reflection of the conducting walls. With the increase of the separatrix angle, the newly formed vorticity pair could be observed within the outflow region (or the plasmoid due to the periodic boundary conditions), which is a driving factor for the formation of the reverse inflow. These factors are more likely to be found in the magnetosphere with a extended current sheet where the plasmoids are frequently detected (Liu et al. 2013; Wang et al. 2016), or in the laboratory reconnection experiments with a limited space (Egedal et al. 2007; Beidler and Cassak 2011; Chandra and Verma 2013). The reverse inflow has been formed gradually during the later stage of reconnection development. Therefore, this type of inflow is most likely to be observed in multiple X-line reconnection. Such reconnection has often been observed in the magnetosphere with a long current sheet. The magnetic structure between any two adjacent X lines is usually called flux rope or magnetic island. If the reconnection at both ends of the flux rope is still active, the two reconnection outflows with opposite directions will be detected within the flux rope (Hasegawa et al. 2010; Øieroset et al. 2011). In some cases, when the two reconnection sites are close to each other, the reconnection outflows may be encountered, thus affecting the magnetic topology of the flux rope (Liu et al. 2017a).

It should be mentioned that the influence of the out-of-plane dynamics on the reconnection inflow has not been considered in the two-dimensional limit, the dynamics could induce current aligned instabilities. In particular, the drift-kink instability (Daughton 1998) has a fast growth rate in a 3D simulation with the reduced ion-electron mass ratio. The lower hybrid drift instability (Daughton et al. 2004) could be more easily driven by the local density gradient. How the out-of-plane dynamics will influence the evolution of reconnection inflow remains to be further explored physically.

Acknowledgements This work was supported by the National Natural Science Foundation of China (grants 41231068, 41531073, 41204127 and 61872047), and the Specialized Research Fund for State Key Laboratories. We acknowledge the use of computer resources at National Space Science Center, CAS. The software used in this work in part developed in pCANS at Chiba University.

References

Angelopoulos, V., McFadden, J.P., Larson, D., Carlson, C.W., Mende, S.B., Frey, H., Phan, T., Sibeck, D.G., Glassmeier, K.-H., Auster, U., Donovan, E., Mann, I.R., Rae, I.J., Russell, C.T., Runov, A., Zhou, X.-Z., Kepko, L.: Tail reconnection triggering substorm onset. Science **321**, 931 (2008)

Beidler, M.T., Cassak, P.A.: Model for incomplete reconnection in sawtooth crashes. Phys. Rev. Lett. **107**, 255002 (2011)

Birn, J., Drake, J.F., Shay, M.A., Rogers, B.N., Denton, R.E., Hesse, M., Kuznetsova, M., Ma, Z.W., Bhattacharjee, A., Otto, A., Pritchett, P.L.: Geospace environmental modeling (GEM) magnetic reconnection challenge. J. Geophys. Res. **106**, 3715 (2001)

Cai, H.J., Lee, L.C.: The generalized Ohm's law in collisionless magnetic reconnection. Phys. Plasmas **4**, 509 (1997)

Chandra, M., Verma, M.K.: Flow reversals in turbulent convection via vortex reconnections. Phys. Rev. Lett. **110**, 114503 (2013)

Daughton, W.: Kinetic theory of the drift kink instability in a current sheet. J. Geophys. Res. **103**, 29429 (1998)

Daughton, W., Lapenta, G., Ricci, P.: Nonlinear evolution of the lower-hybrid drift instability in a current sheet. Phys. Rev. Lett. **93**, 105004 (2004)

Daughton, W., Scudder, J., Karimabadi, H.: Fully kinetic simulations of undriven magnetic reconnection with open boundary conditons. Phys. Plasmas **13**, 072101 (2006)

Egedal, J., Fox, W., Katz, N., Porkolab, M., Reim, K., Zhang, E.: Laboratory observations of spontaneous magnetic reconnection. Phys. Rev. Lett. **98**, 015003 (2007)

Esirkepov, T.Z.: Exact charge conservation scheme for particle-in-cell simulation with an arbitrary form-factor. Comput. Phys. Commun. **135**, 144 (2001)

Fujimoto, K.: Time evolution of the electron diffusion region and the reconnection rate in fully kinetic and large system. Phys. Plasmas **13**, 072904 (2006)

Jin, S.P., Yang, H.A., Wang, X.G.: Hall effect and fine structures in magnetic reconnection with high plasma β. Phys. Plasmas **12**, 042902 (2005)

Harris, E.G.: On a plasma sheath separating regions of oppositely directed magnetic field. Nuovo Cimento **23**, 115 (1962)

Hasegawa, H., Wang, J., Dunlop, M.W., Pu, Z.Y., Zhang, Q.-H., Lavraud, B., Taylor, M.G.G.T., Constantinescu, O.D., Berchem, J., Angelopoulos, V., McFadden, J.P., Frey, H.U., Panov, E.V., Volwerk, M., Bogdanova, Y.V.: Evidence for a flux transfer event generated by multiple X-line reconnection at the magnetopause. Geophys. Res. Lett. **37**, L16101 (2010)

Hoshino, M.: The electrostatic effect for the collisionless tearing mode. J. Geophys. Res. **92**, 7368 (1987)

Huang, Y.-M., Bhattacharjee, A., Sullivan, B.P.: Onset of fast reconnection in Hall magnetohydrodynamics mediated by the plasmoid instability. Phys. Plasmas **18**, 072109 (2011)

Karimabadi, H., Dorelli, J., Roytershteyn, V., Daughton, W., Chacón, L.: Flux pileup in collisionless magnetic reconnection: bursty interaction of large flux ropes. Phys. Rev. Lett. **107**, 025002 (2011)

Lapenta, G.: Self-feeding turbulent magnetic reconnection on macroscopic scales. Phys. Rev. Lett. **100**, 235001 (2008)

Liu, C., Feng, X., Guo, J., Ye, Y.: Study of small-scale plasmoid structures in the magnetotail using Cluster observations and Hall MHD simulations. J. Geophys. Res. **118**, 2087 (2013)

Liu, C., Feng, X., Nakamura, R., Guo, J., Wang, R.: Double-peaked core field of flux ropes during magnetic reconnection. J. Geophys. Res. **122**, 6374 (2017a)

Liu, Y.-H., Hesse, M., Guo, F., Daughton, W., Li, H., Cassak, P.A., Shay, M.A.: Why does steady-state magnetic reconnection have a maximum local rate of order 0.1? Phys. Rev. Lett. **118**, 085101 (2017b)

Lu, Q., Lu, S., Huang, C., Wu, M., Wang, S.: Self-reinforcing process of the reconnection electric field in the electron diffusion region and onset of collisionless magnetic reconnection. Plasma Phys. Control. Fusion **55**, 085019 (2013)

Ma, Z.W., Bhattacharjee, A.: Hall magnetohydrodynamic reconnection: the geospace environment modeling challenge. J. Geophys. Res. **106**, 3773 (2001)

Matthaeus, W.H.: Reconnection in two dimensions: localization of vorticity and current near magnetic X-points. Geophys. Res. Lett. **9**, 660 (1982)

Mandt, M.E., Denton, R.E., Drake, J.F.: Transition to whistler mediated magentic reconnection. Geophys. Res. Lett. **21**, 73 (1994)

Øieroset, M., Phan, T.D., Fujimoto, M., Lin, R.P., Lepping, R.P.: In situ detection of collisionles reconnection in the Earth's magnetotail. Nature **412**, 414 (2001)

Øieroset, M., Phan, T.D., Eastwood, J.P., Fujimoto, M., Daughton, W., Shay, M.A., Angelopoulos, V., Mozer, F.S., McFadden, J.P., Larson, D.E., Glassmeier, K.-H.: Direct evidence for a three-dimensional magnetic flux rope flanked by two active magnetic reconnection X lines at Earth's magnetopause. Phys. Rev. Lett. **107**, 165007 (2011)

Shay, M.A., Drake, J.F.: The role of electron dissipation on the rate of collisionless magnetic reconnection. Geophys. Res. Lett. **25**, 3759 (1998)

Treumann, R.A., Nakamura, R., Baumjohann, W.: Collisionless reconnection: mechanism of self-ignition in thin plane homogeneous current sheets. Ann. Geophys. **28**, 1935 (2010)

Ugai, M.: Self-consistent development of fast magnetic reconnection with anomalous plasma resistivity. Plasma Phys. Control. Fusion **26**, 1549 (1984)

Vasyliunas, V.M.: Theoretical models of magnetic field line merging. Rev. Geophys. **13**, 303 (1975)

Wan, W., Lapenta, G.: Electron self-reinforcing process of magnetic reconnection. Phys. Rev. Lett. **101**, 015001 (2008)

Wang, R., Lu, Q., Nakamura, R., Huang, C., Du, A., Guo, F., Teh, W., Wu, M., Lu, S., Wang, S.: Coalescence of magnetic flux ropes in the ion diffusion region of magnetic reconnection. Nat. Phys. **12**, 263 (2016)

Yang, H.A., Jin, S.P., Zhou, G.C.: Density depletion and Hall effect in magnetic reconnection. J. Geophys. Res. **111**, A11223 (2006)